Miniaturized two-channel broadband spectrometer based on variable-spacing concave blazed gratings

Artem Shcheglov[a], **Yunfeng Nie**[b], **Hugo Thienpont**[b] and **Heidi Ottevaere**[b,*]

[a]Vrije Universiteit Brussel, Department of Applied Physics and Photonics (TONA), Faculty of Engineering, Brussels Photonics (B-PHOT), Brussels, Belgium

[b]Vrije Universiteit Brussel, Department Applied Physics and Photonics (TONA), Faculty of Engineering, Brussels Photonics (B-PHOT) and Flanders Make, Brussels, Belgium

Abstract. Recently, it becomes a tendency for cost-effective, portable spectrometers to have more applications from scientific research to daily life, e.g., in food safety and air pollution analysis. While most spectrometers utilize plane gratings, we demonstrate a more miniaturized, two-channel, broadband spectrometer based on variable-spacing concave gratings, combining the functionality of imaging optics and diffraction grating in one component. The added degree of design freedom in the micro-sized grating spacing further corrects most optical aberrations, thus the design achieves a tiny volume of $<26 \times 12 \times 10$ mm^3 with a high spectral resolution. Simulation results show an optical resolution of <1.6 nm in the VIS-channel (400 to 790 nm) and <3.1 nm in the NIR-channel (760 to 1520 nm). The blazed structure of grating grooves provides a high overall diffraction efficiency in the whole spectral range, more than 50% on average. To further validate the feasibility for mass production, we successfully manufactured the variable-spacing concave gratings by using diamond tooling for fabricating the master mold and hot embossing for replication. Our fabricated variable-spacing grating replicas have a diffraction efficiency up to 70% in the VIS-channel and up to 60% in the NIR-channel. We built the prototype with fabricated concave gratings, and experimental results show a good match (error < 7%) in spectral resolution with the nominal design. [DOI: 10.1117/1.JOM.3.2.024501]

Keywords: broadband miniaturized spectrometer; variable-spacing grating; concave blazed grating; grating mold fabrication and replication.

Paper 22025G received Oct. 17, 2022; accepted for publication Feb. 20, 2023; published online Mar. 13, 2023.

1 Introduction

Portable miniaturized spectrometers are used in a vast variety of applications, such as chemical analysis, astronomy, and environmental monitoring.[1–6] With the applications to more daily life activities, such as food safety[7] and air pollution,[8] the demand to develop cost-efficient, portable spectrometers with a broadband spectrum and high spectral resolution has been increasing.[9–11] To suit the broadband (e.g., covering ultraviolet to near-infrared) requirement, a conventional spectrometer can be a burdensome instrument comprised of a precisely scanning dispersive element and separate imaging optics to achieve both high efficiency and spectral resolution.[12,13] The moving components substantially increase the system's complexity and make it bulky and limited for laboratory use.

State-of-the-art broadband, miniature spectrometers can be categorized into four main categories.[14] The first kind uses narrowband filters to split light into desired spectral bands, e.g., Fabry–Perot can achieve very high spectral resolution while the spectrum is quite narrow, whereas broadband solutions do not provide a spectral resolution higher than 8 to 12 nm.[15,16] The second group disperses light from temporal or spatial interference, then recovers the signal by Fourier transform (FT), hence FT spectrometers. Their spectral resolution is limited by the maximum optical path difference, resulting in a moderate resolution (~7.5 nm) from reported

*Address all correspondence to Heidi Ottevaere, heidi.ottevaere@vub.be

broadband devices.[17] The third group obtains the spectral information by computational reconstruction of chromatic images, of which 2.1-nm resolution has been reported in the spectral range from 400 to 900 nm.[18] However, it requires a complex calibration procedure and is highly sensitive to temperature fluctuations and vibrations.

The last group utilizes dispersive gratings to get spatially separated spectra. Due to the maturity in design algorithms and fabrication techniques, plane gratings are most frequently used in portable spectrometers and provide a high spectral resolution from 1 to 3 nm in a broad spectral range.[19,20] Recent advances in grating fabrication with almost any groove shape bring up the concave grating designs, which introduces more degrees of freedom for aberration correction and ensures a more compact structure. The volume of a concave-grating-based microspectrometer is only $11 \times 6 \times 5$ mm^3,[21] with a 5 nm resolution in a spectral range from 400 to 1030 nm. However, it is based on a multi-order concept and requires sequential illumination of the target with light sources of limited spectral ranges. Cheng et al.[22] presented a high-resolution, broadband single-photon dispersive spectrometer using concave grating; nevertheless, it needs a highly cooled, bulky, expensive superconducting nanowire detector. In 2017, Chen et al.[23] reported a concave grating spectrometer with a volume of 360 cm^3 and a resolution better than 1.5 nm from 360 to 825 nm. Such a relatively high optical resolution is achieved by utilizing a concave grating with variable spacing.

Like other gratings, concave gratings also have inherent constraints such as a limited free spectral range due to high-order spectral overlapping and low diffraction efficiencies for broadband usage. To overcome these issues and at the same time employ the advantages of a concave grating, we propose a variable-spacing concave grating with a two-channel design to broaden the spectral range and compensate for the low efficiency of using only one grating. With the development in diamond tooling and high-precision replication techniques, the fabrication of such gratings has become more available.

In the following section, we present the optical design method for the two-channel, variable-spacing concave grating. By introducing variable spacing on the concave grating, the optical aberrations are well compensated. We divide the broad spectrum into VIS and NIR channels without adding movable components to achieve a high spectral resolution and efficiency. Furthermore, gratings have an optimized blazed structure to maximize the overall diffraction efficiency. In Sec. 3, we investigate the mass-fabrication strategies for the designed variable-spacing concave gratings. The assembled spectrometer and the obtained experimental results are discussed in Sec. 4. Finally, the conclusions are drawn, and future work is discussed.

2 Optical Design

Recently, we reported the design of the miniaturized spectrometer,[24,25] where a broad spectral range was divided into two channels. In that design, we use two plane gratings, and all the components are off-the-shelf products, which limits the volume to be further minimized. In this work, we further simplify the optical layout by replacing plane gratings with concave gratings, greatly reducing the optical volume by more than 60%.

2.1 *Optical Configuration*

The layout of the proposed optical design is shown in Fig. 1. The incoming light consequently goes through an entrance slit (size of 15×500 μm^2) and a mechanical aperture (NA = 0.1), which reduces the amount of stray light in the system. Then, an achromatic doublet lens (COMAR 08DQ06) collimates the light in a broadband spectral range. A dichroic beamsplitter (Semrock FF775) and a flat mirror have been placed to keep one entrance port for both channels and the possibility of one detector. The beamsplitter can reflect light from 400 to 790 nm and transmits light in 760- to 1520-nm spectrum, respectively the VIS-channel and the NIR-channel. The two channels have concave gratings with different spacing and blazed structures for high efficiency, while they are placed in one plane to be fabricated using one mold, as described in Sec. 3. The optical layout of the spectrometer is limited to an optical volume of $26 \times 12 \times 10$ mm^3.

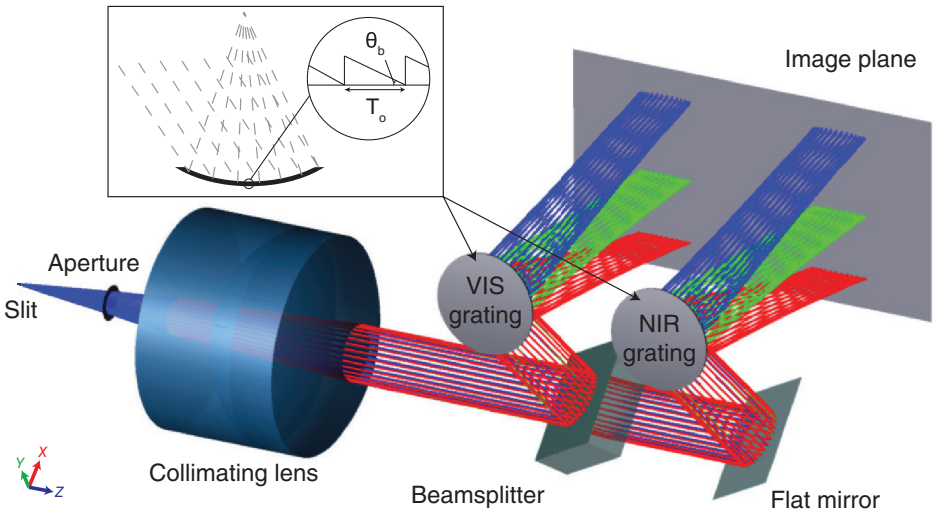

Fig. 1 Optical configuration overview. The blue, green, and red rays correspond to 400, 600, and 760 nm in the VIS-channel and to 775, 1200, and 1520 nm in the NIR-channel, respectively. The inset schematically sketches the curved grating with the blazed structure, where T_0 is the grating spacing and θ_b is the blazed angle.

For detection, we plan to use a 2D SONY IMX990 sensor sensitive in a broad spectral range from 400 to 1700 nm. A 2D sensor allows using one detector for two spectral channels by acquiring the signal separately from two parts of the sensor. Furthermore, a 2D sensor helps to soften the tolerances for fabrication and assembly of a miniaturized spectrometer since light is not constrained to be well-focused inside the pixel height as in the case of a line sensor.

2.2 *Concave Grating Design Method*

The concave grating combines an elliptical surface sag and a diffraction grating with grooves that can have a variable spacing across the grating surface.[26] The sag z of such a grating is given as

$$z = \frac{cu^2}{1 + \sqrt{1 - u^2}}, \tag{1}$$

where

$$u^2 = a^2x^2 + b^2y^2. \tag{2}$$

In these equations, x, y, and z are the surface coordinates, and a, b, and c are the coefficients that define the shape of the elliptical substrate.

By controlling the groove spacing along the grating surface, one can change the form of the meridional focal curve of the grating, which defines the point spread function along the dispersion axis of the grating.[6] In other words, it has a direct impact on the spectral resolution of the spectrometer. The effective grating spacing is defined as follows:

$$d_{\text{eff}} = T_0 + \alpha y + \beta y^2, \tag{3}$$

where T_0 is the default spacing at the center of the grating, and α and β are the polynomial coefficients, defining the grooves aperiodicity across the grating surface.

The gratings were designed in Zemax OpticStudio using Elliptical Grating 1 surface type and optimized with a custom merit function based on the XENC operand.[26] This operand computes the distance to the specified fraction of the extended source encircled energy. As an extended source, we used an entrance slit with a width of 15 μm. The goal of the optimization was to minimize the full-width-half-maximum (FWHM) of the encircled energy distribution along the

Table 1 Overview of the designed variable-spacing concave diffraction grating parameters.

	VIS-grating	NIR-grating
Surface sag parameters		
b	0.053	0.053
c	18.874	18.914
Grating parameters		
T_0 (μm)	0.909	1.818
α	$5.23 * 10^{-4}$	$3.48 * 10^{-3}$
β	$2.59 * 10^{-3}$	$4.14 * 10^{-3}$

dispersion axis at the detector plane. Table 1 provides an overview of the optimized grating parameters.

The coefficient a controls the substrate curvature in the plane parallel to the groove lines. This curvature determines the sagittal focal curve and does not impact the spectral resolution of the system. Hence, the coefficient a was set to zero, ensuring that the gratings are flat along their x-axis, which considerably simplifies the grating fabrication as described in Sec. 3. Figures 2(a) and 2(b) illustrate the surface sag of both gratings. Both gratings have almost an identical

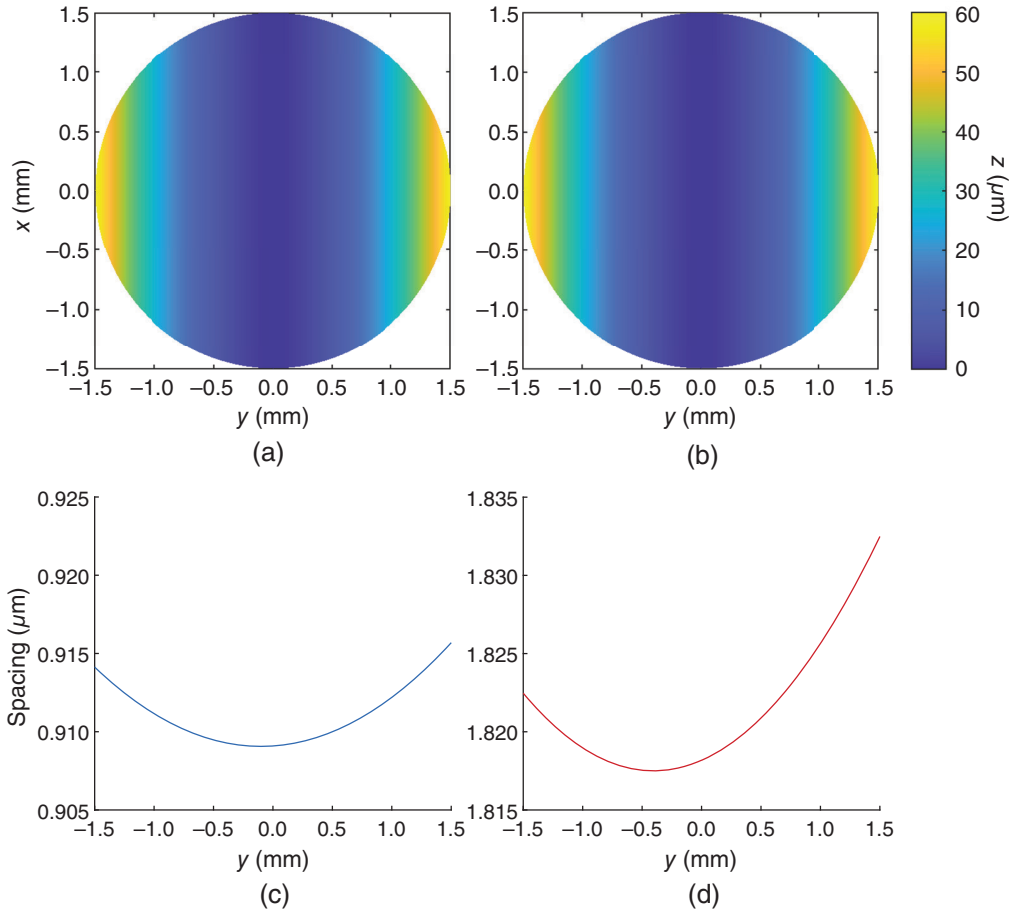

Fig. 2 Variable-spacing concave gratings design. Surface sag for the (a) VIS- and (b) NIR-grating. Variable grating spacing sectional distribution at $x = 0$ mm for the (c) VIS- and (d) NIR-grating.

aspherical shape with a slight difference in the c coefficient. The maximum surface sag for both gratings is 60 μm, on a circular aperture of 3-mm diameter.

As seen in Table 1, the NIR-grating spacing T_0 is twice that of the VIS-grating. It is defined in such a way as to provide an identical diffraction angle for the central wavelengths in both spectral channels, which makes the light follows a similar optical path from the grating toward the sensor. As a result, the two channels will focus on the same sensor, considerably simplifying the optical layout. Figures 2(c) and 2(d) demonstrate the spacing distribution of the two gratings. Both gratings have a parabolic spacing distribution with the vertex located in a non-zero y-coordinate. The gratings have a bigger spacing at the edge that corresponds to the positive values of y-coordinates (upper part of the gratings in Fig. 1).

The image obtained in Zemax OpticStudio after ray tracing has been performed in the proposed optical layout as shown in Fig. 3(a). Both spectral channels are captured by the same sensor, each occupying half of the sensor without overlapping with the neighboring channel.

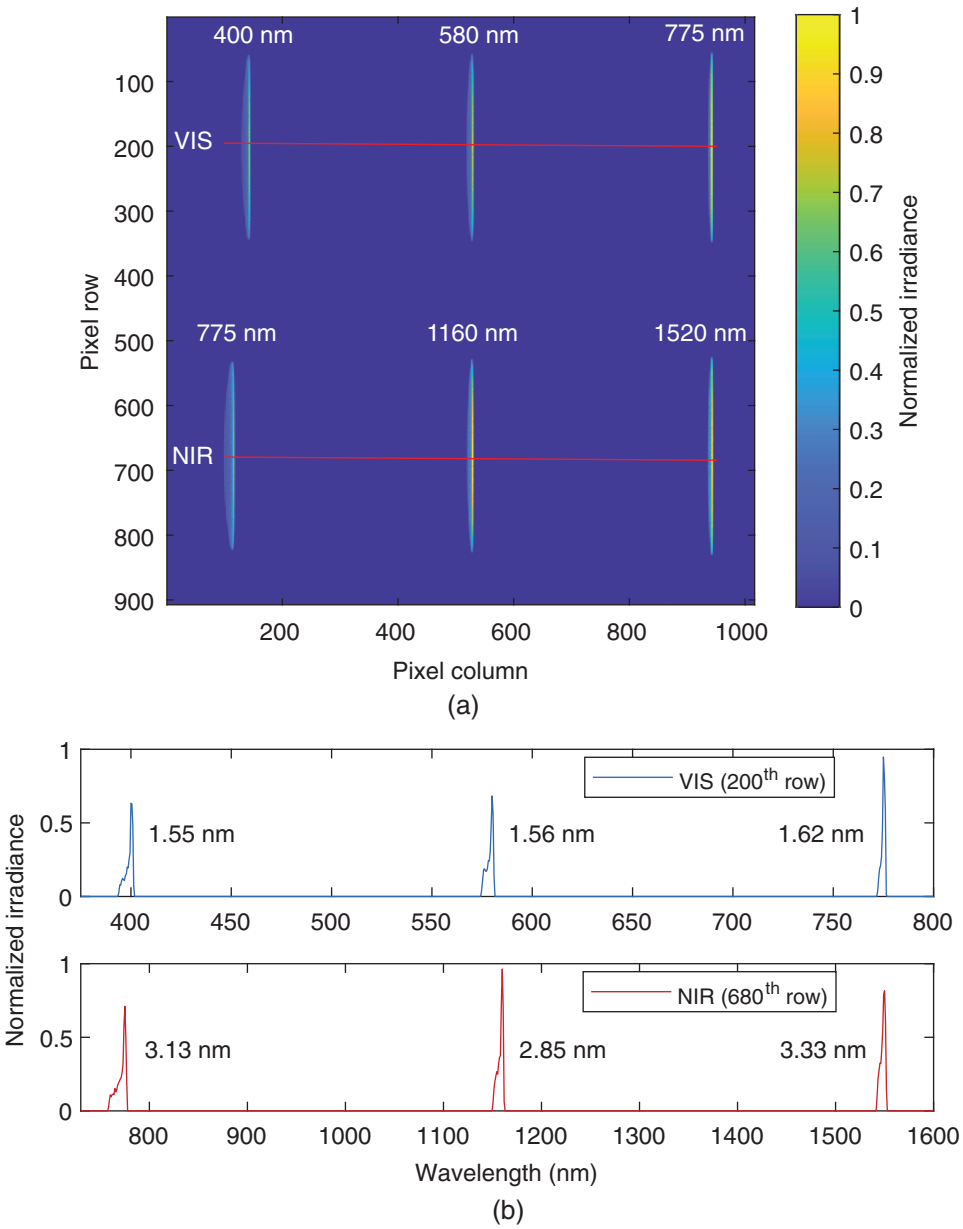

Fig. 3 (a) Spectral image simulation with six predefined wavelengths. The red lines demonstrate the cross-section readout. (b) The FWHM values in the cross-section indicate the spectral resolution at the corresponding wavelengths.

The simulated spectral peaks are shown in Fig. 3(b). The spectral FWHM data are calculated from the central row of each channel on the sensor, as depicted by the red lines in Fig. 3(a). Averaging signals of all the rows along the wavelength footprint can improve the signal-to-noise ratio (SNR) performance, which has been demonstrated in our previous work.[24] The spectral peaks are asymmetrical due to the residual coma and field curvature aberrations. However, it has a minor impact on the spectral resolution. Simulations show that the mean spectral resolution in the VIS-channel is 1.6 nm, while in the NIR-channel, it is 3.1 nm.

2.3 *Blazed Structure and Diffraction Efficiency Estimation*

While the imaging performance is determined by the surface sag along with the grating spacing, the shape of the grooves defines the diffraction efficiency that is critical for the final SNR. The diffraction efficiency is defined as the ratio between the power diffracted into a designated direction and the power incident on the grating. In the case of the proposed optical configuration, the designated direction is the range of diffraction angles corresponding to wavelengths of VIS- and NIR- spectral channels in the chosen diffraction order (+1). One of the approaches to control and direct the power into the desired spectral range is based on the groove shape called blazed or sawtooth grating. Blazed gratings are usually characterized by a triangular groove shape with a blaze angle θ_b, as depicted in the inset of Fig. 1. The blaze angle θ_b is controlled and optimized for the best spectral performance.

To define the required blaze angle for both gratings, we used the diffraction equation solved for the blaze angle θ_b:

$$\theta_b = \arcsin\left(\frac{m\lambda}{2T_0}\right), \tag{4}$$

where m is the diffraction order and λ is the blaze wavelength, which theoretically has the highest diffraction efficiency. Since the blaze wavelength has a high efficiency, we chose 600 nm for the VIS-channel and 1200 nm for the NIR-channel for a more balanced efficiency over the whole spectral range. It resulted in a blaze angle of 19.3 deg for both gratings.

We chose three coordinates (the center and two edges) on the surface to estimate the diffraction efficiency of the designed grating, as seen in Table 2. The angle of incidence θ_i with respect to a local normal differs depending on the surface coordinate, influencing the grating efficiency. Furthermore, the blaze angle θ_b changes along the grating surface since the angle of the diamond tool is fixed with respect to the substrate normal during the whole diamond tooling process. Thus, the three chosen coordinates sample the minimum, the maximum and the medium conditions for calculating the grating efficiency.

The grating efficiency is calculated using rigorous Fourier modal methods in VirtualLab Fusion. The input parameters are the local blazed angle θ_b and the light incidence angle θ_i. Preliminary simulations showed that small changes in the grating spacing, <0.02 μm/mm as shown in Figs. 2(c) and 2(d), have negligible impacts on the grating efficiency (changes <1%). Therefore, the grating spacing was kept equal to T_0 for the three simulations. Unpolarized light was assumed and approximated as the average of two orthogonal polarization states $(\mathrm{TE} + \mathrm{TM})/2$. The efficiency model utilized an aluminum coating, providing a high reflectivity in the whole working range of the spectrometer.

Table 2 Simulation conditions. #1, #2, and #3 correspond to the three chosen coordinates along the grating surface (the center and two edges).

	y (mm)	θ_i (deg)	θ_b (deg)
#1	−1.5	45.9	23.9
#2	0.0	41.3	19.3
#3	1.5	37.0	14.7

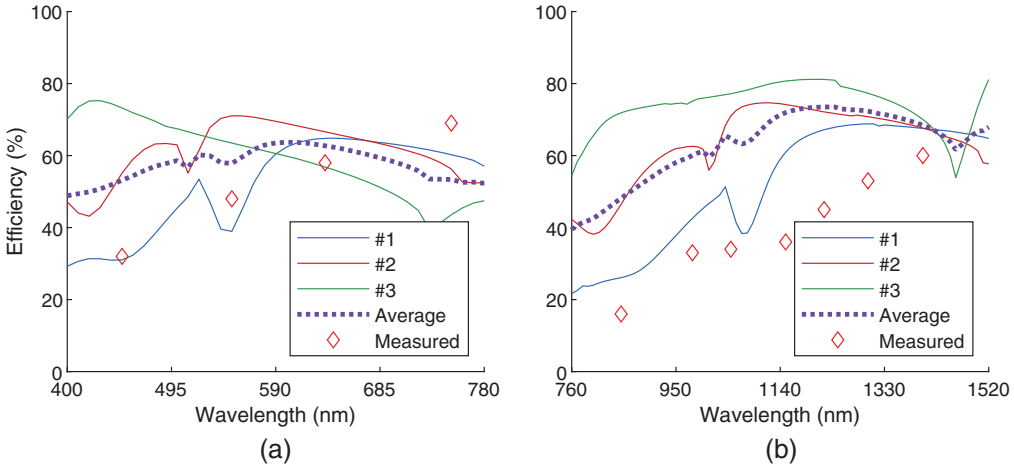

Fig. 4 Diffraction efficiency simulation and measurements for the (a) VIS and (b) NIR gratings. The standard deviation is lower than 3% for all measured values. #1, #2, and #3 correspond to the three coordinates along the grating surface (the center and two edges) chosen for the efficiency simulation.

Figure 4 illustrates the simulated diffraction efficiencies for the VIS- and NIR- gratings. As can be seen, the peak efficiency shifts toward shorter wavelengths as the y-coordinate changes from negative to positive values. This shift occurs due to the blaze angle θ_b changing across the grating surface, which results in a different blaze wavelength λ. Moreover, gratings have a higher overall efficiency level at the edge that corresponds to positive y-coordinates. It can be explained by the shadowing effect when part of the incoming light falls on the sidewall of the grating groove. This effect is more present at the edge of the grating that corresponds to negative y-coordinates, where sidewalls face a more significant part of the incoming light due to the local curvature.

Given that the diffraction efficiency of the whole grating is the contribution of all grooves, we approximated it as an average of the three conditions. The average efficiencies are shown in Figs. 4(a) and 4(b) with bold dotted lines. As a result, the VIS-grating has a diffraction efficiency of more than 50% in the designed spectral range from 400 to 790 nm. The NIR-grating provides a diffraction efficiency higher than 40% in the spectral range from 760 to 1520 nm and higher than 50% from 900 to 1520 nm. The measurements of the fabricated gratings are described in Sec. 3.

3 Grating Fabrication and Replication

Mass production can significantly reduce the grating cost since direct tooling of a periodical structure is both time- and cost-consuming. To manufacture the gratings in mass production, two steps are generally needed, the fabrication of a master mold followed by replication.

Direct methods used to fabricate periodical structures include direct ruling, holography, photolithography, and electron beam writing. However, fabricating blazed structures on spherical or aspherical substrates using these methods can be challenging and typically involves multistage processing.[27,28] It has been demonstrated that ultra-precision diamond tooling is a suitable technique for processing advanced optical surfaces,[29–31] including the fabrication of free-form blazed gratings.[32–34] Xu et al.[35] used ultra-precision diamond tooling to cut a convex reflective variable spacing grating with a blazed structure and a grating density of 300 lines/mm. The grating was used in the Offner configuration covering a spectral range from 500 to 1100 nm. In another work, Li et al.[36] diamond tooled a convex spherical blazed grating with 54 lines/mm grating density. According to the reported simulations, this grating can provide an efficiency higher than 50% in the spectral range from 1650 to 2500 nm.

In this work, the master mold was produced using a Moore Nanotechnology 350 FG machine capable of 5-axis ultraprecision diamond tooling. We selected a brass plate for the mold substrate

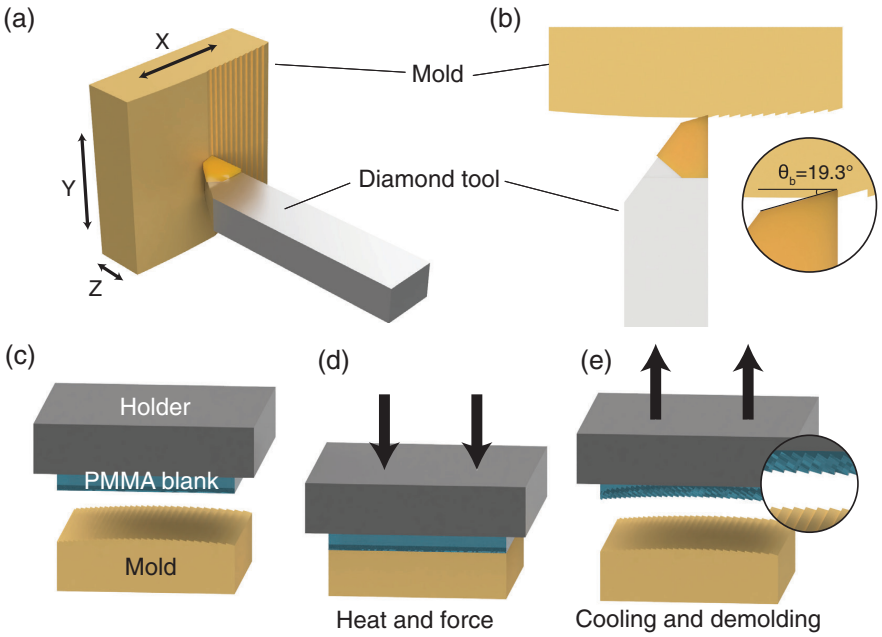

Fig. 5 Variable spacing concave blaze grating fabrication. Diamond tooling of grating grooves on a convex substrate: (a) three-dimensional and (b) top views. Hot embossing of grating replicas: (c) general overview prior to the embossing; (d) embossing with force and temperature applied; and (e) cooling and demolding of a final replica.

with a 1-mm NiP coating. In the first stage, we used diamond tooling to shape the aspherical base of the gratings. Since the mold is used afterwards for grating replication, the shape of the base should be opposite of the sag profile shown in Fig. 2. Therefore, the base shape of the grating mold is convex.

Figures 5(a) and 5(b) schematically illustrate the diamond tooling process of the grating grooves. The diamond tool is fixed, and the workpiece with a mounted brass plate moves vertically along the *Y*-axis to remove material, thus cutting the grating profile. The workpiece moves along the *X*-axis to cut every new groove, whereas the *Z*-axis brings the tip of the diamond tool to the correct sag position. For this ruling process, we used a diamond tool with an excluded angle of 18.25 deg. We introduced an additional tilt with respect to the substrate normal so that the diamond tool has an angle corresponding to the designed blazed angle of 19.3 deg, as shown in the inset in Fig. 5(b).

Figure 6 shows the picture of the fabricated mold. The VIS- and NIR- gratings were positioned next to each other, so that both gratings can be replicated simultaneously in one replication step. The dashed circles in the inset of Fig. 6 show the clear aperture of the gratings, the diameter of which is equal to 3 mm, and the rest of the grating surface is cut due to the diamond tool evacuation. After the mold was successfully fabricated, we produced several replicas of the gratings in polymethyl methacrylate (PMMA) through hot embossing. Hot embossing is the technique of imprinting microstructures on a substrate using a mold under a given pressure and molding temperature. Along with injection molding, it has proven to be one of the best methods for manufacturing micro-component on a mass scale.[37–41] Figures 5(c), 5(d), and 5(e) illustrate the basic principle of hot embossing. First, a PMMA blank is mounted onto a holder so that the blank can be effectively brought into contact with the mold. Secondly, the mold is pressed into a heated PMMA blank. This way, the mold's structure is transferred into a replica. Finally, the PMMA blank is cooled down, and demolding takes place.

The fabricated mold and replicated samples were examined using SEM. Figure 7 shows the analysis results. Both the mold and replicated gratings have a repeatable periodical structure. Figure 8 shows a comparison between AFM-profiles of the mold and one of the replicated samples both for the VIS- and NIR- gratings. The mold profile of the VIS-grating has unexpected waviness in the valleys of the grooves, which is also visible in the profile of the measured replica,

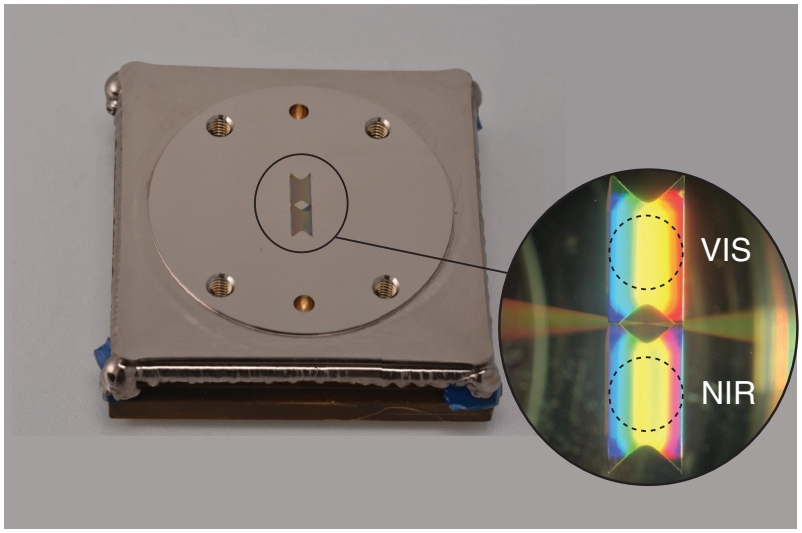

Fig. 6 The fabricated two-channel grating mold using diamond tooling. The inset demonstrates the picture of the VIS and NIR gratings taken with an optical microscope. Dashed lines show the clear aperture of the gratings.

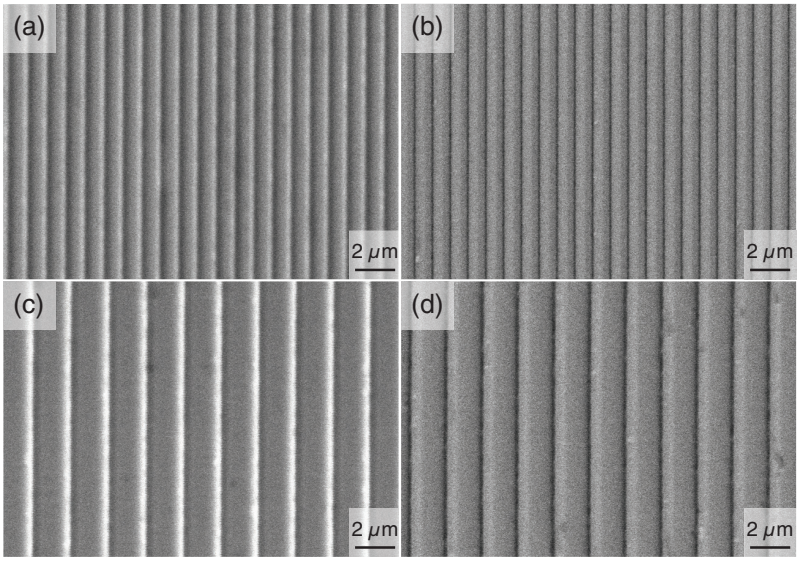

Fig. 7 SEM analysis. VIS-grating: (a) mold and (b) replica. NIR-grating: (c) mold and (d) replica.

where this effect is transferred to the peaks of the grooves. Most probably, it was caused by the damage of the diamond tool. This effect is not present in the profile of the NIR-grating because it was cut first, whereas the damage, as we assume, occurred during the diamond tooling of the VIS-grating. The replica profile of the NIR-grating is in good agreement with the mold profile. However, the peaks of the replica's grooves have a more rounded shape compared with the mold. One of the possible reasons is that the PMMA blank was not sufficiently immersed in the mold. Additional simulations have shown that such deviations from the ideal grating profile can result in an efficiency drop up to 10% both for VIS- and NIR- grating. Further investigation and optimization of diamond tooling and hot embossing processes are required to achieve a better match between a replica and the ideal blazed profile.

After replication, we sputtered the samples with a thin layer of reflective aluminum coating. We measured the diffraction efficiency of the fabricated samples, which is defined as the ratio between the power diffracted into the designated diffraction order and the power incident on the grating. The efficiency was performed with the gratings installed into the spectrometer housing

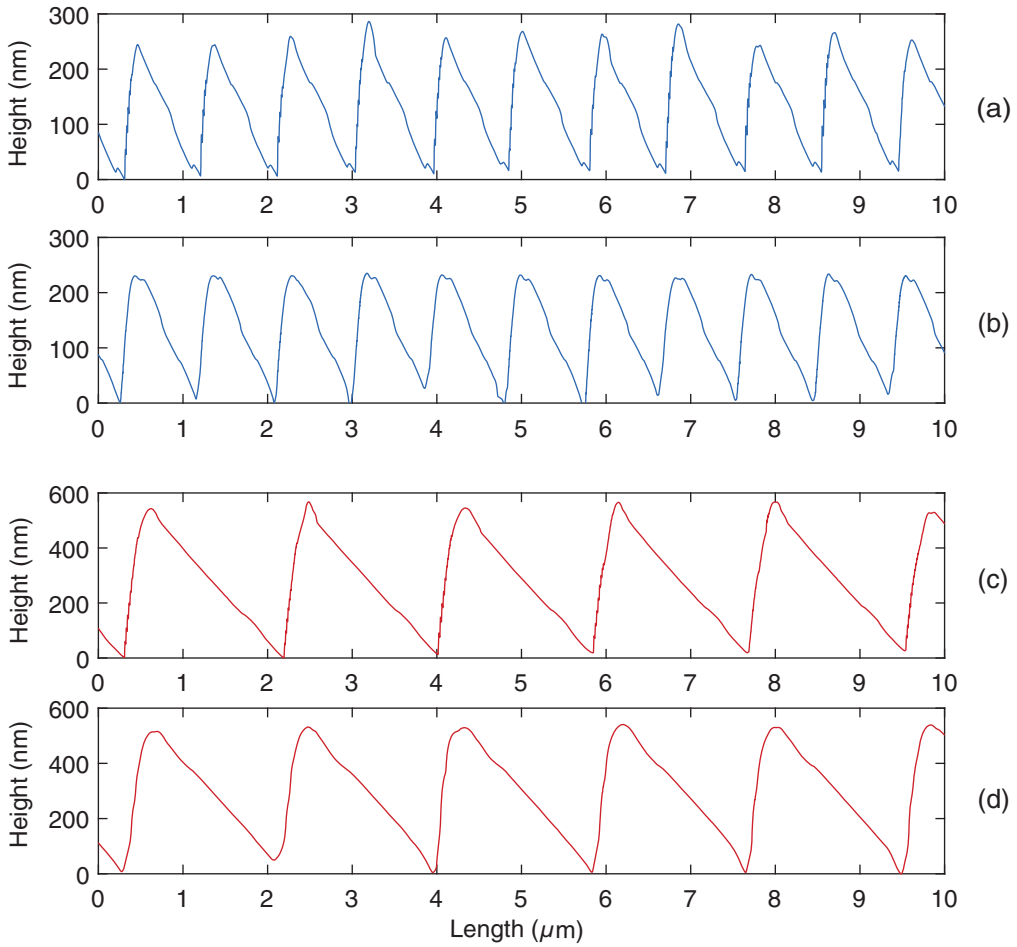

Fig. 8 AFM characterization. VIS-grating: (a) mold and (b) replica. NIR-grating: (c) mold and (d) replica.

described in Sec. 4.1. To provide monochromatic illumination of the gratings, we used a set of dichroic bandpass filters. The efficiency results of the measurements are shown in Fig. 4 along with the simulation values. The VIS-grating reaches a maximum diffraction efficiency of 70%, whereas the blaze wavelength is larger than the one in the simulations. Most probably, it is caused by misalignments that occurred during the assembly of the prototype. As a result, the beam at the grating surface could be shifted toward the edge, corresponding to the blaze wavelength in the region 630 to 680 nm (simulation condition #1). The NIR-grating achieves a maximum diffraction efficiency of 60%. In addition to a small shift of the blaze wavelength, an overall drop in efficiency exists due to the fabrication deviation from the nominal grating profile.

4 Prototyping and Characterization

4.1 *Prototype Description*

To make sure the prototype achieves the designed spectral resolution, we have performed a tolerance analysis as described in our previous work based on flat gratings.[24] It has been shown that the XYZ-decenter tolerance and XYZ-tilt of all optical components do not exceed ±0.1 mm ±0.5 deg, respectively. Therefore, all the tolerances are within a commercial class, and no higher precision tolerance class is required.[42,43]

The broadband sensor used in the design has not been yet released for purchase as an off-the-shelf device. Therefore, we designed two separate housings for two different sensors to provide a proof-of-concept demonstration for the whole spectral range from 400 to 1520 nm. In the first

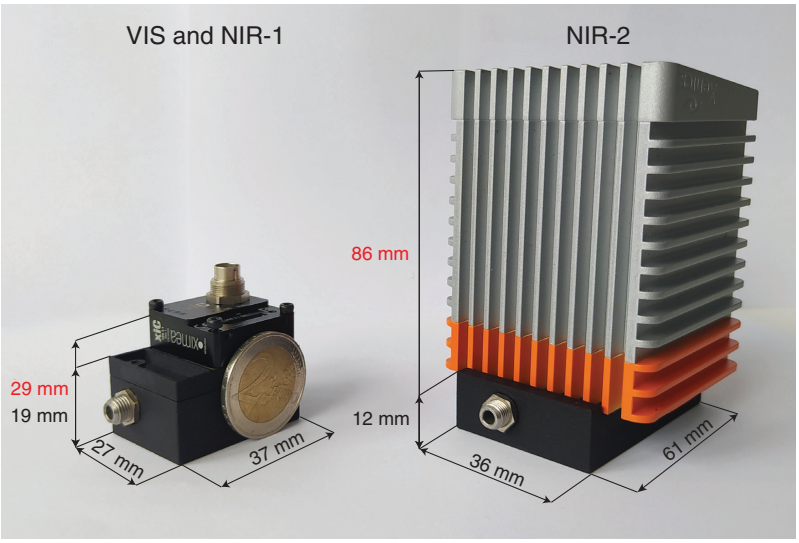

Fig. 9 The assembled spectrometers. The red values correspond to the height including the cameras' housings sizes.

case, we used a camera from XIMEA with Sony IMX225 sensor sensitive in a spectral range from 400 to 1000 nm. Therefore, it covers the whole spectral range of the VIS-channel and a part of the NIR-channel, namely from 760 to 1000 nm (hereinafter referred to as NIR-1). This sensor has a pixel pitch of 3.45 μm and a diagonal of 16.1 mm, so no modifications in the previously proposed design were required. To demonstrate the capabilities of the proposed design in the whole NIR-channel, we used a Xenics Bobcat 320 camera based on an InGaAs sensor sensitive in a spectral range from 900 to 1700 nm (hereinafter referred to as NIR-2). The sensor has a diagonal of 8.2 mm and a pixel size of 20 μm. Figure 9 shows the picture with the assembled spectrometers.

The mechanical housings for both demonstrators were printed using multi-jet fusion technology that provides sufficient accuracy and resolution for fast prototyping of such optical systems The housing consists of two parts printed separately and later assembled with cameras through threaded joints. The mechanical aperture, lens, and replicas with concave gratings are glued within the designed holders printed as one part with the spectrometer housing. The entrance slit is glued on the SMA bulkhead adapter. This adapter has one degree of freedom (along the z-axis in Fig. 1), so that by moving an entrance slit, an optimal focal position can be found.

As shown in Fig. 9, the spectrometer housing designed for the VIS and NIR-1 channels has a size of $37 \times 29 \times 27$ mm^3, whereas for the NIR-2 channel is $61 \times 36 \times 12$ mm^3. The bigger size of the second housing is due to the specific arrangement of the threaded holes in the camera's body, which were used for assembly with the spectrometer housing.

4.2 *Experimental Results*

To characterize the performance of the proposed design, we used the Ar-Hg source that provides distinctive spectral lines from 300 to 1600 nm. The source was used as well to perform a calibration, i.e. to relate the pixel number to wavelength.

The spectra acquired after calibration are shown in Fig. 10, whereas the comparison between the simulated and measured numerical FWHM values of the spectral peaks is provided in Table 3. The simulated values in Table 3 are obtained using the pixel sizes of the used sensors. The change in pixel size (compared to the simulations shown in Sec. 2.1) does not affect the spectral resolution in the VIS and NIR-1 channels, as it is smaller than the pixel size of the original design. However, in the NIR-2 channel, the pixel pitch increased to 20 μm, leading to a deterioration of the predicted spectral resolution. It comes from the entrance slit image being integrated by bigger pixels. For example, the simulated spectral resolution at 1295 nm has increased from 3.71 to 6.28 nm.

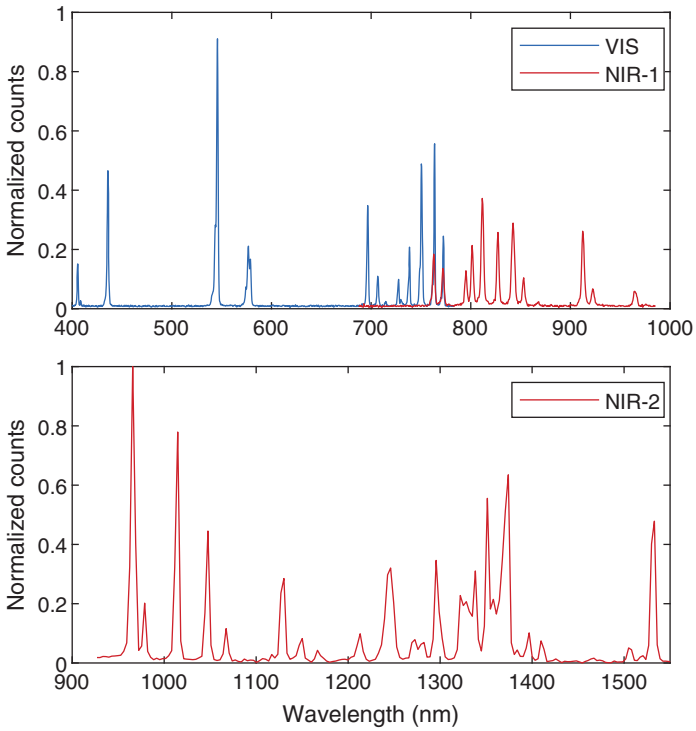

Fig. 10 The measured spectrum of Ar-Hg source using the (a) SONY and (b) Bobcat sensors.

Table 3 The comparison of the spectral resolution achieved through simulations and measurements. The simulated values are obtained using the actual pixel pitches of the used sensors. It is noteworthy that the NIR-2 sensor has a lower resolution due to a bigger pixel size (20 μm) compared to the design (3.45 μm).

Spectral channel	Spectral line (nm)	Simulated (nm)	Measured (nm)
VIS	435.833	1.56	1.60
	546.074	1.53	1.79
	750.387	1.66	1.71
NIR-1	811.531	3.02	2.98
	912.297	3.48	3.07
NIR-2	965.779	5.63	5.02
	1295.666	6.28	6.23
	1532.934	6.42	6.32

The experimental results presented in Table 3 demonstrate that the optical resolution in the VIS, NIR-1, and NIR-2 channels are in good agreement with the performed simulations. The measured mean spectral resolution is 1.7 and 3 nm for the VIS and NIR-1 channels, respectively. In the NIR-2 channel, we achieved a mean resolution of 5.9 nm. However, in this channel, we expect a resolution comparable to the NIR-1 channel if a sensor with a smaller pixel (e.g., 3.45 μm, compared to the current 20 μm) size is used.

5 Conclusions

In this work, we have designed and demonstrated a miniaturized, two-channel, broadband spectrometer on concave gratings with variable line spacing. The suggested optical design maintains

the advantage of concave grating spectrometers in terms of compactness and simplicity while effectively expanding the spectral band, outperforming other reported concave-grating spectrometers. By combining concave gratings with the two-channel concept, this spectrometer achieves a broad spectral range from 400 to 1520 nm with a miniature optical volume of $26 \times 12 \times 10$ mm^3. Simulation results show a resolution smaller than 1.6 nm in the VIS-channel and smaller than 3.1 nm in the NIR-channel. The concave gratings have an optimized blazed structure that provides a diffraction efficiency higher than 40% throughout the working range of the spectrometer.

We investigated a possible mass-production strategy of the two-channel concave grating by using diamond tooling for mold fabrication and hot embossing for replication. The fabricated replicas have a repeatable structure and show a maximum diffraction efficiency up to 70% in the VIS-channel and up to 60% in the NIR-channel. Experiments on the assembled prototype demonstrate that the resolutions in VIR- and NIR-channels are both in good agreement with the optical design results (error in the optical resolution $< 7\%$).

The proposed design combines the advantages of having a high optical resolution and broad spectral range in one device, while maintaining the size of the spectrometer sufficiently compact. Such capabilities benefit spectrometric analysis and increase versatility for potential applications. In future studies, we plan to optimize the fabrication process of the variable-spacing concave grating so that the diffraction efficiency can be improved and brought closer to the theoretical estimations.

Acknowledgments

This work was supported by European Union's Horizon 2020 Research and Innovation program under the Marie Sklodowska-Curie Action (765635, xCLASS), Fonds Wetenschappelijk Onderzoek (FWO 1252722N), and Vrije Universiteit Brussel (Hercules, Methusalem, OZR). The authors would like to thank Dries Rosseel, Jef Verbaenen, and Sergey Verlinski for their support in performing the grating fabrication.

Code, Data, and Materials Availability

The data generated in this work is available from the corresponding author upon reasonable request.

References

1. D. S. Goldman, P. White, and N. Anheier, "Miniaturized spectrometer employing planar waveguides and grating couplers for chemical analysis," *Appl. Opt.* **29**(31), 4583–4589 (1990).
2. G. Cataldo et al., "Micro-spec: an ultracompact, high-sensitivity spectrometer for far-infrared and submillimeter astronomy," *Appl. Opt.* **53**(6), 1094–1102 (2014).
3. Z. Li et al., "Design of a flat field concave-grating-based micro-Raman spectrometer for environmental applications," *Appl. Opt.* **51**(28), 6855–6863 (2012).
4. M. M. Mariani, P. J. Day, and V. Deckert, "Applications of modern micro-Raman spectroscopy for cell analyses," *Integr. Biol.* **2**(2-3), 94–101 (2010).
5. K.-L. Wei et al., "The design and experiment of multi-parameter water quality monitoring microsystem based on MOEMS microspectrometer," *Spectrosc. Spectral Anal.* **32**(7), 2009–2014 (2012).
6. E. G. Loewen and E. Popov, *Diffraction Gratings and Applications*, CRC Press (2018).
7. H. Mohamed et al., "Use of near and mid infra-red spectroscopy for analysis of protein, fat, lactose and total solids in raw cow and Camel milk," *Food Chem.* **334**, 127436 (2021).
8. L. Cotrozzi et al., "Reflectance spectroscopy: a novel approach to better understand and monitor the impact of air pollution on mediterranean plants," *Environ. Sci. Pollut. Res.* **25**(9), 8249–8267 (2018).

9. Hamamatsu, "Hamamatsu FTIR engine C15511-01," https://www.hamamatsu.com/us/en/product/optical-sensors/spectrometers/ftir-engine/C15511-01.html (accessed 2022-05-10).
10. A. Emadi et al., "Design and implementation of a sub-nm resolution microspectrometer based on a linear-variable optical filter," *Opt. Express* **20**(1), 489–507 (2012).
11. W. Hartmann et al., "Waveguide-integrated broadband spectrometer based on tailored disorder," *Adv. Opt. Mater.* **8**(6), 1901602 (2020).
12. Teledyne Princeton Instruments, "SpectraPro® HRS. High performance imaging spectrometers," https://www.princetoninstruments.com/products/spectrapro-family/spectra-pro-hrs (accessed 2021-02-22).
13. HORIBA, "MicroHR Series," https://www.horiba.com/en_en/products/detail/action/show/Product/microhr-series-1591/ (accessed: 2022-02-22).
14. Z. Yang et al., "Miniaturization of optical spectrometers," *Science* **371**(6528), eabe0722 (2021).
15. J. Antila et al., "MEMS and piezo actuator-based Fabry–Perot interferometer technologies and applications at VTT," *Proc. SPIE* **7680**, 76800U (2010).
16. M. Ebermann et al., "Tunable mems Fabry-Pérot filters for infrared microspectrometers: a review," *Proc. SPIE* **9760**, 97600H (2016).
17. Y. M. Eltagoury, Y. M. Sabry, and D. A. Khalil, "All-silicon double-cavity fourier-transform infrared spectrometer on-chip," *Adv. Mater. Technol.* **4**(10), 1900441 (2019).
18. P. Wang and R. Menon, "Computational spectroscopy via singular-value decomposition and regularization," *Opt. Express* **22**(18), 21541–21550 (2014).
19. Avantes, "AvaSpec-Mini2048CL," https://www.avantes.com/products/spectrometers/compactline/avantes-spectrometer-mini-2048cl/ (accessed 2022-09-07).
20. Ocean Insight, "Ocean Insight microspectrometers," https://www.oceaninsight.com/products/spectrometers/microspectrometer/ (accessed 2022-09-07).
21. R. Brunner et al., "Microspectrometer based on holographically recorded diffractive elements using supplementary holograms," *Opt. Express* **16**(16), 12239–12250 (2008).
22. R. Cheng et al., "Broadband on-chip single-photon spectrometer," *Nat. Commun.* **10**(1), 1–7 (2019).
23. J. Chen et al., "High-resolution compact spectrometer based on a custom-printed varied-line-spacing concave blazed grating," *Opt. Express* **25**(11), 12446–12454 (2017).
24. A. Shcheglov et al., "Miniaturized cost-effective broadband spectrometer employing a deconvolution reconstruction algorithm for resolution enhancement," *Opt. Express* **30**(7), 11459–11471 (2022).
25. A. Gasser et al., "Miniaturized time-resolved fluorescence spectrometer system," *Proc. SPIE* **12008**, 120080B (2022).
26. Zemax, *Zemax OpticStudio 22.1. User Manual*, Zemax (2022).
27. D. W. Wilson et al., "Recent advances in blazed grating fabrication by electron-beam lithography," *Proc. SPIE* **5173**, 51730E (2003).
28. P. D. Maker et al., "New convex grating types manufactured by electron beam lithography," in *Diffractive Opt. and Micro-Opt.*, Optica Publishing Group, p. DWD–3 (1998).
29. F. Fang et al., "Manufacturing and measurement of freeform optics," *CIRP Ann.* **62**(2), 823–846 (2013).
30. Q. Liu, H. Thienpont, and H. Ottevaere, "Freeform-based high numerical aperture optics for confocal raman/sers spectroscopy," in *Freeform Opt.*, Optical Society of America, p. RW1A–3 (2021).
31. Z. Xiong et al., "Design and optimization method of a convex blazed grating in the offner imaging spectrometer," *Appl. Opt.* **60**(2), 383–391 (2021).
32. C. De Clercq et al., "Elois: an innovative spectrometer design using a free-form grating," *Proc. SPIE* **9626**, 96261O (2015).
33. M. Davies et al., "Diamond machining of diffraction gratings for imaging spectrometers," *Precis. Eng.* **36**(2), 334–338 (2012).
34. C. B. Lee and S. K. Lee, "Fabrication and molding testing of the blazed gratings for micro-optics applications," *Key Eng. Mater.* **447–448**, 396–400 (2010).
35. D. Xu et al., "Design, fabrication, and testing of convex reflective diffraction gratings," *Opt. Express* **25**(13), 15252–15268 (2017).

36. H. Li et al., "Ultra-precision cutting and characterization of reflective convex spherical blazed grating elements," *Micromachines (Basel)* **13**(7), 1115 (2022).
37. D. V. Rosato and M. G. Rosato, *Injection Molding Handbook*, Springer Science & Business Media (2012).
38. C. Lee et al., "Optimizing the fabrication process of a high-efficiency blazed grating through diamond scribing and molding," *J. Micromech. Microeng.* **20**(5), 055028 (2010).
39. S. S. Deshmukh and A. Goswami, "Hot embossing of polymers–a review," *Mater. Today:. Proc.* **26**, 405–414 (2020).
40. J. Van Erps et al., "Prototyping and replication of polymer freeform optical components," in *Opt. Fabric. and Test.*, Optica Publishing Group, p. OM4B–2 (2017).
41. S. S. Deshmukh and A. Goswami, "Recent developments in hot embossing–a review," *Mater. Manuf. Process.* **36**(5), 501–543 (2021).
42. R. R. Shannon, *Tolerancing Techniques*, ch. 36, McGraw-Hill (1995).
43. E. Milby, *Tolerancing Optical Systems*, Academic Press (2009).

Artem Shcheglov is a researcher at the Faculty of Engineering of the Vrije Universiteit Brussel (VUB) since 2018. He holds a BSc degree in telecommunications and an MSc degree in optical systems and communication networks, both from ITMO University (St. Petersburg, Russia). He completed his PhD in February 2023 at VUB, where he worked on "Next-Generation Miniaturized Spectroscopic Systems" under the guidance of Prof. Dr. Ir. Heidi Ottevaere and Dr. Ir. Yunfeng Nie. His research involved the development of miniaturized spectrometers, as well as the design and replication of diffractive optical elements.

Yunfeng Nie is a full-time researcher at the Faculty of Engineering of the VUB since 2014. She obtained her BSc degree in mechanical engineering from the University of Science and Technology of China (USTC) and an MSc degree in optical engineering from the University of Chinese Academy of Sciences (UCAS). She pursued her PhD in the topic of "advanced free-form optical imaging system" in the VUB under EU's FP7 Marie Curie Programme 'ADOP-SYS' with exchanges in LPI company (Spain) and FSU University (Germany). She has been very active in freeform optical design algorithms, imaging spectrometers and biomedical imaging for more than 10 years.

Hugo Thienpont is a full professor at the Faculty of Engineering of the VUB. He is director of Brussels Photonics B-PHOT, the photonics research group at the VUB, which he built over the years and which today counts more than 70 photonics researchers, engineers, technical experts and administrative staff. He graduated as an electrotechnical engineer with majors in applied physics in 1984 and obtained his PhD in applied sciences in 1990, both at the VUB. Since 2012, he has been vice-rector for Innovation and Industrial policy at the VUB.

Heidi Ottevaere is a full professor at the Faculty of Engineering of the VUB since October 2009. Since 2019, she chairs the Applied Physics and Photonics Department (TONA) of the Faculty of Engineering that is responsible for the Photonics Education Curriculum at Vrije Universiteit Brussel. She is responsible for the Instrumentation and Metrology platform at the Photonics Innovation Center and for the biophotonics research unit of the Brussels Photonics Team B-PHOT.